

Cite this: *Chem. Sci.*, 2024, 15, 2167

All publication charges for this article have been paid for by the Royal Society of Chemistry

# Facile electrocatalytic proton reduction by a [Fe–Fe]-hydrogenase bio-inspired synthetic model bearing a terminal CN<sup>−</sup> ligand†

Abhijit Nayek,<sup>†a</sup> Subal Dey,<sup>†a</sup> Suman Patra,<sup>a</sup> Atanu Rana,<sup>a</sup> Pauline N. Serrano,<sup>b</sup> Simon J. George,<sup>bd</sup> Stephen P. Cramer,<sup>bcd</sup> Somdatta Ghosh Dey<sup>\*,a</sup> and Abhishek Dey<sup>\*,a</sup>

An azadithiolate bridged CN<sup>−</sup> bound pentacarbonyl bis-iron complex, mimicking the active site of [Fe–Fe] H<sub>2</sub>ase is synthesized. The geometric and electronic structure of this complex is elucidated using a combination of EXAFS analysis, infrared and Mössbauer spectroscopy and DFT calculations. The electrochemical investigations show that complex **1** effectively reduces H<sup>+</sup> to H<sub>2</sub> between pH 0–3 at diffusion-controlled rates (10<sup>11</sup> M<sup>−1</sup> s<sup>−1</sup>) i.e. 10<sup>8</sup> s<sup>−1</sup> at pH 3 with an overpotential of 140 mV. Electrochemical analysis and DFT calculations suggests that a CN<sup>−</sup> ligand increases the pK<sub>a</sub> of the cluster enabling hydrogen production from its Fe(II)–Fe(0) state at pHs much higher and overpotential much lower than its precursor bis-iron hexacarbonyl model which is active in its Fe(0)–Fe(0) state. The formation of a terminal Fe–H species, evidenced by spectroelectrochemistry in organic solvent, via a rate determining proton coupled electron transfer step and protonation of the adjacent azadithiolate, lowers the kinetic barrier leading to diffusion controlled rates of H<sub>2</sub> evolution. The stereo-electronic factors enhance its catalytic rate by 3 order of magnitude relative to a bis-iron hexacarbonyl precursor at the same pH and potential.

Received 11th October 2023  
Accepted 22nd December 2023

DOI: 10.1039/d3sc05397k

rsc.li/chemical-science

Hydrogenases (H<sub>2</sub>ases) efficiently interconvert H<sup>+</sup> to H<sub>2</sub> with high turnover numbers (TONs) (10<sup>2–5</sup> mol s<sup>−1</sup>).<sup>1,2</sup> Based on the metal centers present at the active site of these metalloenzymes, three types of H<sub>2</sub>ases are known in nature – [Fe–Fe] H<sub>2</sub>ase, [Ni–Fe] H<sub>2</sub>ase and Fe-only H<sub>2</sub>ase.<sup>3,4</sup> Among these, the [Fe–Fe] H<sub>2</sub>ases are more selective towards H<sub>2</sub> generation, the [Ni–Fe] H<sub>2</sub>ases are selective for H<sub>2</sub> oxidation while the Fe-only H<sub>2</sub>ases in the presence of a hydride acceptor/donor substrate reacts with H<sub>2</sub> or produce H<sub>2</sub>.<sup>5,6</sup> High-resolution X-ray crystal structure of the that [Fe–Fe] H<sub>2</sub>ase active site reveals that one of the iron centers of a Fe<sub>2</sub>S<sub>2</sub>(CO)<sub>3</sub>(CN)<sub>2</sub> organometallic core (2Fe subsite) is attached to a [Fe<sub>4</sub>S<sub>4</sub>] cluster through a bridging cysteine (Scheme 1A and B).<sup>4,7,8</sup> A key bismethyleneazadithiolate (ADT) moiety bridges between the two Fe centers of the Fe<sub>2</sub>S<sub>2</sub>(CO)<sub>3</sub>(CN)<sub>2</sub> organometallic core. Each of the two iron centers are coordinated with one –CO ligand and one –CN<sup>−</sup> ligand.<sup>9,10</sup> A –CO ligand bridges both

of the iron centers (Scheme 1A and B).<sup>7,11</sup> The catalytic cycle of [Fe–Fe] H<sub>2</sub>ases encompasses three primary oxidation states. These include H<sub>ox</sub> (oxidized), characterized by a Fe(II)–Fe(II) [Fe<sub>4</sub>S<sub>4</sub>]<sup>2+</sup> state;<sup>12,13</sup> H<sub>red</sub> (reduced), denoting a Fe(II)–Fe(I) [Fe<sub>4</sub>S<sub>4</sub>]<sup>2+</sup> state; and H<sub>sred</sub> (super reduced), which manifests as a Fe(II)–Fe(I) [Fe<sub>4</sub>S<sub>4</sub>]<sup>+</sup> state.<sup>14–16</sup> The unique catalytic capability of the H-cluster is attributed, among other factors, to a distinctive arrangement known as the rotated structure. This configuration introduces a vacant site at the distal iron (Fe<sub>d</sub>) atom.<sup>17–21</sup> The proposed mechanism suggests that the initial protonation occurs at the bridgehead nitrogen atom of the Fe(II)–Fe(I) state within the enzyme.<sup>14,22</sup> A critical step in this process involves a proton relay from the bridgehead –NH group to the distal iron atom (Fe<sub>d</sub>). This step is considered pivotal in the formation of a terminal hydride species with a amine form of the ADT bridgehead, H<sub>hyd</sub>, which is characterized as a superoxidized diiron site with Fe(II)–Fe(II) state.<sup>23–27</sup> Substrates (H<sup>+</sup>/H<sub>2</sub>) along with the inhibitors like O<sub>2</sub> and CO, binding occurs at the distal iron centre (Fe<sub>d</sub>).<sup>17,20</sup> The synthesis and characterization of [Fe–Fe] H<sub>2</sub>ase mimic has become a rapidly growing area of research.<sup>28–37</sup> A large number of [Fe–Fe] H<sub>2</sub>ase active site analogues have been synthesized mimicking several structural aspects of the active site and several details of electronic structure and its contribution to reaction mechanism have been elucidated.<sup>30,31,37–41</sup> In particular, the role of the μ-CO ligand and

<sup>a</sup>School of Chemical Science, Indian Association for the Cultivation of Science, Kolkata 700032, India. E-mail: icsgd@iacs.res.in; icad@iacs.res.in

<sup>b</sup>Department of Chemistry, University of California, Davis, CA 94616, USA

<sup>c</sup>Physical Biosciences Division, Lawrence Berkeley National Laboratory, Berkeley, CA 94720, USA

<sup>d</sup>SETI Institute, 339 Bernardo Ave, Suite, 200 Mountain View, CA 94043, USA

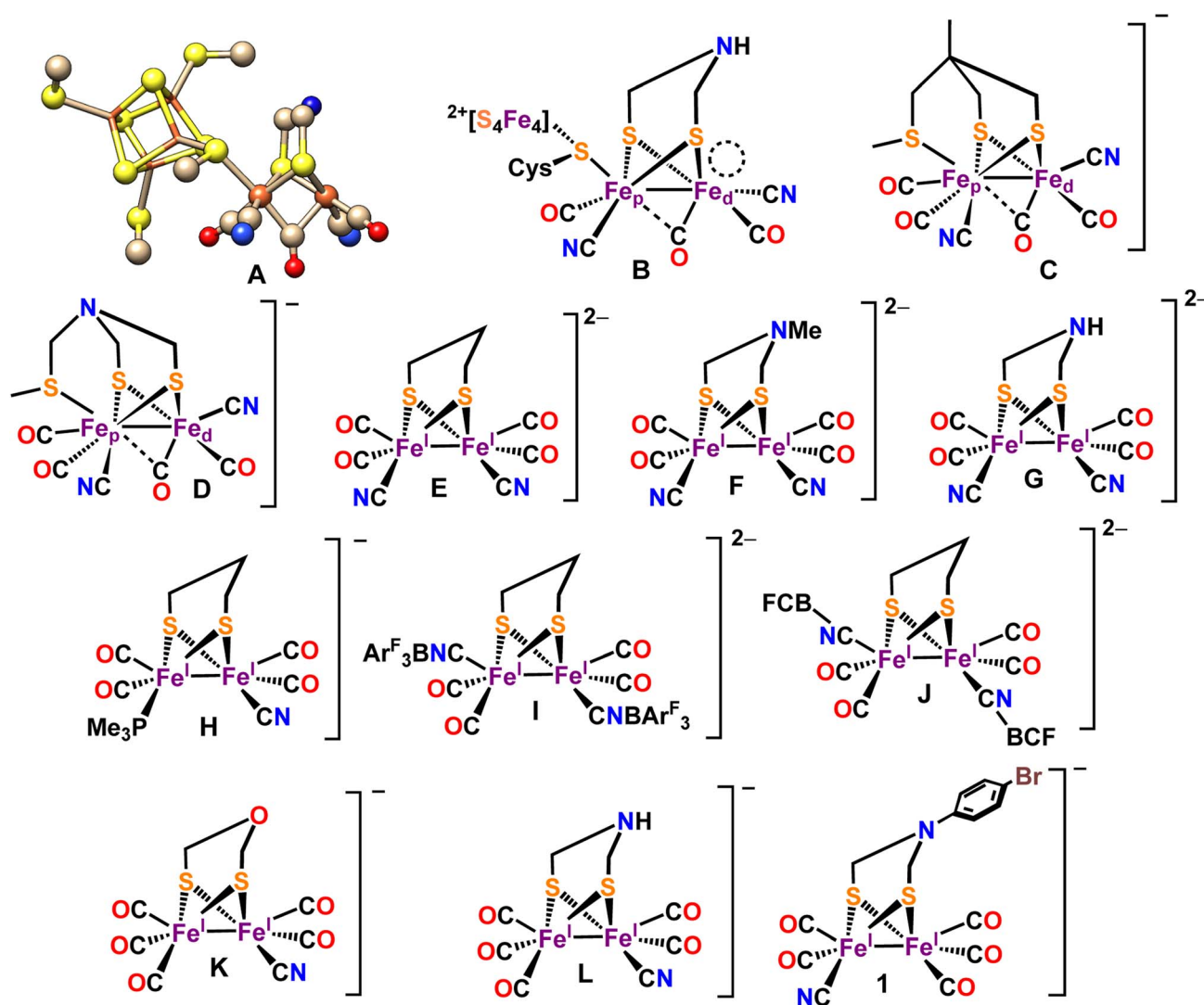
† Electronic supplementary information (ESI) available. See DOI: <https://doi.org/10.1039/d3sc05397k>

‡ These authors contributed equally to this work.

the rotated structure of the core has been a matter of great interest. After the initial report of a transient  $-\text{CO}$  bridged  $\text{Fe}(\text{I})$ – $\text{Fe}(\text{II})$  complex,<sup>42</sup> synthetic model complexes with  $\mu$ - $\text{CO}$  ligands have been reported.<sup>28,39,43</sup> Similarly, mimics of 2Fe subsite with  $\text{CN}^-$  ligands and Lewis acid capped  $\text{CN}^-$  ligands have been reported (Scheme 1C–L).<sup>44–54</sup>

Lately, there has been several reports that it's possible to activate the  $[\text{Fe}–\text{Fe}]$   $\text{H}_2$ ases enzyme by introducing synthetic complexes with  $-\text{CN}^-$  ligands to the apo-enzyme (which has different bridging dithiolate ligands).<sup>55–60</sup> Recently, the formation of a miniaturized  $[\text{Fe}–\text{Fe}]$   $\text{H}_2$ ases incorporating  $-\text{CN}^-$  ligands, has been reported. This model is generated through the combination of an oligopeptide binding  $[\text{Fe}_4\text{S}_4]$  cluster and an organometallic Fe complex, and its formation has been scrutinized using various spectroscopic techniques.<sup>61</sup> The electrocatalytic and photocatalytic behaviour for some of these synthetic analogues of  $[\text{Fe}–\text{Fe}]$   $\text{H}_2$ ases were reported mostly in organic solvents.<sup>46,61,63–69</sup> In a report by our group, a synthetic

model  $p\text{-BrC}_6\text{H}_4\text{N}(\text{CH}_2\text{S})_2\text{Fe}_2\text{CO}_6$  was shown to be a very efficient catalyst for HER under aqueous condition.<sup>70</sup> This catalyst exhibited TON and TOF of  $>>10^8$  and  $6400\text{ s}^{-1}$  at 440 mV overpotential. Following this, several recent reports of HER by  $\text{Fe}_2\text{S}_2(\text{CO})_6$  complexes have appeared in the literature.<sup>71–73</sup> The same  $p\text{-BrC}_6\text{H}_4\text{N}(\text{CH}_2\text{S})_2\text{Fe}_2\text{CO}_6$  model has been used to investigate the mechanism of degradation of the  $\text{Fe}_2\text{S}_2(\text{CO})_6$  cluster in the presence of  $\text{O}_2$ .<sup>74</sup> Using these insights synthetic analogues of  $[\text{Fe}–\text{Fe}]$   $\text{H}_2$ ases which could catalyze HER in the presence of  $\text{O}_2$  were developed.<sup>75</sup> However, these complexes did not bear terminal  $\text{CN}^-$  ligands present in the active site of  $\text{H}_2$ ase which plays a major role in the reactivity of  $[\text{Fe}–\text{Fe}]$   $\text{H}_2$ ase.<sup>47,76</sup> Synthetic models bearing terminal  $\text{CN}^-$  ligands have been reported and their ability to catalyze HER has been evaluated.<sup>47,52,53,77–79</sup> However, these complexes decomposed in the presence of acid *via* protonation of the electron rich  $\text{CN}^-$  ligand and produced sub-stoichiometric  $\text{H}_2$ .<sup>80</sup> Thus, the role of  $\text{CN}^-$  ligand in HER catalysis remains unexplored in synthetic models.



**Scheme 1** (A) X-ray crystal structure of the "H-cluster" in the  $\text{H}_{\text{ox}}$  state in  $[\text{Fe}–\text{Fe}]$ - $\text{H}_2$ ase (PDB ID: 3C8Y<sup>62</sup>). (B) Chem Draw representation of the active site of  $[\text{Fe}–\text{Fe}]$ - $\text{H}_2$ ase. The vacant site at the distal iron atom is indicated by a circular ring. Reported  $[\text{Fe}–\text{Fe}]$   $\text{H}_2$ ase synthetic mimics bearing  $-\text{CN}$  ligands in  $\text{H}_{\text{rest}}$  (C–L). New synthetic mimic of  $[\text{Fe}–\text{Fe}]$   $\text{H}_2$ ase  $[\text{BrC}_6\text{H}_4\text{N}(\text{CH}_2\text{S})_2\text{Fe}_2(\text{CO})_5\text{CN}]^-$  (1).



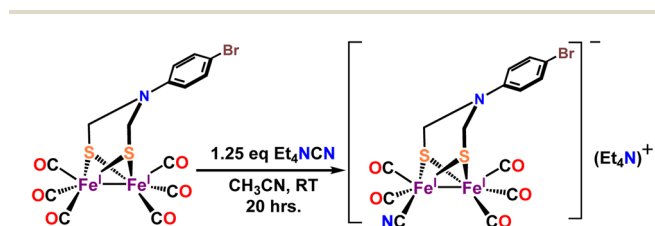
In this manuscript, we have substituted a terminal  $-\text{CO}$  of a synthetic mimic  $p\text{-BrC}_6\text{H}_4\text{N}(\text{CH}_2\text{S})_2\text{Fe}_2(\text{CO})_6$  by a  $\text{CN}^-$  leading to a ADT bridge synthetic mimic of the  $\text{H}_{\text{red}}$  state,  $[\text{Et}_4\text{N}]^+[\text{BrC}_6\text{H}_4\text{N}(\text{CH}_2\text{S})_2\text{Fe}_2(\text{CO})_5\text{CN}]^-$  (**1**, Scheme 1). The geometric and electronic structure of complex **1** is elucidated by EXAFS, FTIR, ESI-MS, Mössbauer,  $^1\text{H}$ -NMR and DFT calculations. The heterogeneous electrochemical hydrogen production with the complex **1** has been investigated in dil.  $\text{H}_2\text{SO}_4$  ( $\text{pH} \leq 3$ ) solution and the results indicate hydrogen production at very low overpotential with very high turnover rates orders of magnitude greater than those obtained for the precursor complex which does not bear the terminal  $\text{CN}^-$  ligand. While the  $\text{CN}^-$  ligand, remaining intact during electrolysis both in aqueous and organic solvents, shifts the reduction potentials more cathodic, it activates the  $\text{Fe}(\text{I})\text{-Fe}(\text{0})$  state for HER catalysis

which results in a much lower overpotential for HER relative to the precursor complex which requires reduction to the  $\text{Fe}(\text{0})\text{-Fe}(\text{0})$  state for HER catalysis.

## Results and analysis

### Synthesis and characterization

Complex **1** is synthesized *via* modification of a previously reported literature method.<sup>52</sup> Addition of 1.25 eq. of  $\text{Et}_4\text{NCN}$  under dark to the precursor complex  $p\text{-BrC}_6\text{H}_4\text{N}(\text{CH}_2\text{S})_2\text{Fe}_2(\text{CO})_6$  in dry acetonitrile led to gradual change of color from red to reddish brown (Scheme 2). FTIR spectrum was measured after 7–8 h. That showed disappearance of vibrations for the precursor complex and appearance of several new vibrations, especially  $2093\text{ cm}^{-1}$  band (Fig. 1A, red). The band gradually increased in intensity and the final product was isolated after 24 h. The detailed experimental procedure is described in the ESI.† The composition of the product was determined using  $^1\text{H}$ -NMR (Fig. S10†),  $^{13}\text{C}$ -NMR (Fig. S11†), elemental analysis, negative mode Mass spectrometry (Fig. 1B) and Mössbauer spectroscopy (Fig. 2B). In particular, the mass spectrum showed a fragmentation pattern consistent with the loss of five  $-\text{CO}$  ligands present in the complex (Fig. 1B). Complex **1** showed  $\lambda_{\text{max}}$  at 358 nm with weaker transitions at 529 nm, 428 nm and 286 nm (Fig. S1†). The transitions below 400 nm likely represent



Scheme 2 Synthetic route for complex **1**.

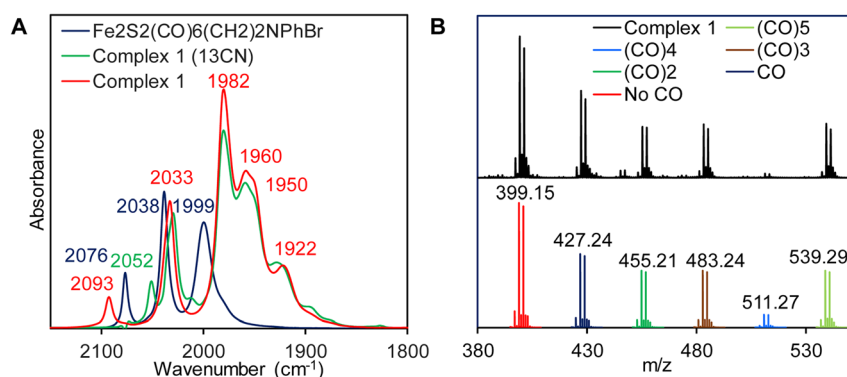


Fig. 1 (A) FTIR spectra for complex **1** (red) & its  $^{13}\text{C}$ N analogue (green). The precursor complex is shown in blue (B)  $(-)$  ve ion mode ESI-MS of complex **1** (black) and corresponding simulated spectra with successive five  $\text{CO}$  release (bottom).

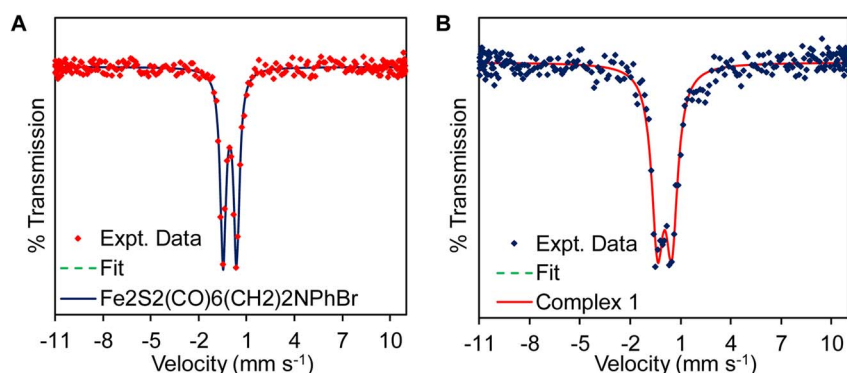


Fig. 2 Mössbauer spectra of the (A) precursor complex and (B) complex **1** recorded at 90 K.

Fe  $\rightarrow$  CO MLCT transitions. On replacing one CO in  $p\text{-BrC}_6\text{H}_4\text{N}(\text{CH}_2\text{S})_2\text{Fe}_2(\text{CO})_6$  complex with  $\text{CN}^-$  in complex **1**, these Fe  $\rightarrow$  CO MLCT transitions were shifted to lower energies. This is consistent with increase in the d manifold due to reduction of  $Z_{\text{eff}}$  because of the  $\text{CN}^-$  ligation.

The  $p\text{-BrC}_6\text{H}_4\text{N}(\text{CH}_2\text{S})_2\text{Fe}_2\text{CO}_6$  complex showed characteristic C–O vibrations at 2076, 2038 and 1999  $\text{cm}^{-1}$  (Fig. 1A, blue). These vibrations were shifted to lower energies to 2033, 1982, 1960, 1950 and 1922  $\text{cm}^{-1}$  in complex **1** (Fig. 1A, red). The terminal  $\nu_{\text{CO}}$  vibrations of the  $\text{CN}^-$  bound complex **1** were red shifted relative to the neutral complex which indicates enhanced Fe–CO back bonding in the anionic complex relative the neutral complex. The presence of a terminal  $\text{CN}^-$  ligand in complex **1** was inferred from the vibration at 2093  $\text{cm}^{-1}$  in the FTIR which shift to lower wavenumbers upon incorporation of  $^{13}\text{CN}^-$  to 2052  $\text{cm}^{-1}$  (Fig. 1A, green). These results are well in agreement with the previously reported synthetic models of  $\text{H}_2\text{ases}$  bearing terminal  $\text{CN}^-$  ligand and attributes complex **1** as terminally bound mono  $\text{CN}^-$  substituted pentacarbonylated  $[\text{2Fe}]$ -subsite models.<sup>50,81,82</sup>

The presence of  $\text{CN}^-$  in complex **1** was also suggested by Mössbauer spectroscopy (Fig. 2) of the precursor complex and complex **1**. The precursor complex has an isomer shift ( $\delta_{\text{iso}}$ ) and quadruple splitting ( $\Delta E_{\text{Q}}$ ) of  $-0.051 \text{ mm s}^{-1}$  and  $0.846 \text{ mm s}^{-1}$  consistent with a Fe(I)–Fe(I) electronic structure description.<sup>83</sup> The  $\delta_{\text{iso}}$  and  $\Delta E_{\text{Q}}$  for complex **1** is  $0.05 \text{ mm s}^{-1}$  and  $0.85 \text{ mm s}^{-1}$ , respectively. Due to the presence of anionic  $\text{CN}^-$  in complex **1**, the electron density in the diiron cluster increases and as a result the  $\delta_{\text{iso}}$  of the complex **1** shift to slightly more positive values (Fig. 2B and Table 1) compared to the precursor complex,  $\text{Fe}_2\text{S}_2(\text{CO})_6(\text{CH}_2)_2\text{NPhBr}$  (Fig. 2A and Table 1). These results are consistent with the previous reported values of  $\text{CN}^-$  bound complexes.<sup>49,83</sup>

In order to obtain structural parameters, several attempts to grow X-ray suitable single crystal were unsuccessful. Hence, EXAFS data of an acetonitrile solution of complex **1** are obtained at the Fe K-edge. The Fourier transform spectrum is dominated by 3 sets of peaks (Fig. 3). The strong peak at about 2.28 Å fits well to an average of 2 Fe–S interactions per Fe. At shorter distance, the peaks around 1.7–1.9 Å arise from Fe–C interactions. Detailed fitting reveals that these interactions can be separated into 2 groups, with about half occurring at an average of 1.74 Å, and the rest averaging about 1.89 Å, indicating that apart from the Fe–CN some of the Fe–CO's have longer Fe–C bond lengths. A scattering from the nitrogen of the  $\text{CN}^-$  ligand can be clearly picked up at 3.1 Å, indicating the presence of the  $\text{CN}^-$  ligand. Finally, the

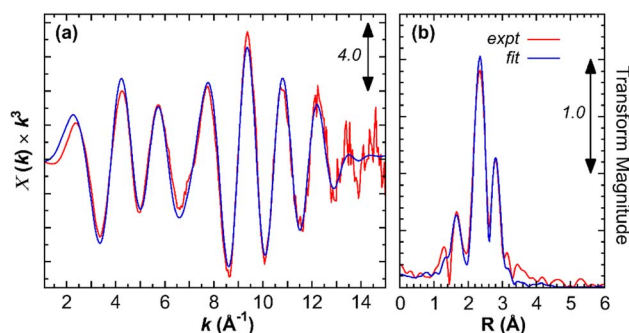


Fig. 3 Fe K-edge EXAFS spectra of complex **1**. (a) EXAFS data (red) and fit (blue). (b) Corresponding Fourier transform spectra.

Table 2 The bond distances obtained from the Fourier transformed EXAFS data

Interaction	$N^a$	$R$ (Å)	$\sigma^2$ (Å <sup>2</sup> )	$\Delta E^0$ (eV)
Fe–S	2.0	2.280 (0.003)	0.0049 (0.0002)	–8.7(0.3)
Fe–C	1.5	1.738 (0.004)	0.0030 (0.0003)	
	1.5	1.878 (0.005)	0.0031 (0.0005)	
Fe–O (CO)	2.0	2.916 (0.003)	0.0045 (0.0002)	
Fe–N	0.5	3.106 (0.009)	0.0020 (0.0002)	
Fe–Fe	1.0	2.489 (0.002)	0.0037 (0.0006)	

<sup>a</sup>  $N$  = Number of backscattering atoms;  $R$  = distance;  $\sigma^2$  = Debye–Waller factor;  $\Delta E^0$  = threshold energy. In this fit, the backscatter atom numbers ( $N$ ) are fixed to the values expected for the model while  $R$ ,  $\sigma^2$ , and  $\Delta E^0$  are floated. Threshold energies ( $\Delta E^0$ ) are constrained to be the same for all components. The estimated uncertainties in  $R$ ,  $\sigma^2$ , and  $\Delta E^0$  are shown in parentheses. Parameters without uncertainties in parentheses were not floated in the given fit. The scale factor used was 1.0. Phase and amplitudes were calculated using FEFF8.42.

analysis indicates the presence of a Fe–Fe interaction at 2.49 Å (Table 2).

Geometry optimized density functional theory (DFT)<sup>84–86</sup> calculations are used to deduce a possible three-dimensional structure of the complex **1** pre-assuming the fact that the complex bears five –CO and a  $\text{CN}^-$  ligand along with the ADT as indicated from the above spectroscopic characterizations.<sup>55,87,88</sup> DFT calculations were used to validate the experimentally obtained structural and vibrational features to emulate the feasibility of -axial and -equatorial conformers (Fig. 4B and C) (where the  $\text{CN}^-$  ligand is either -axial or -equatorial with respect to the plane defined by the ADT moiety, *i.e.*  $\text{Fe}_2\text{S}_2$  plane) (Fig. 4). The calculations at this level could reproduce the three-dimensional geometry and vibrational frequencies of the precursor complex reasonably (Table 3).<sup>70</sup> These calculations indicate that while both the conformers result in stable geometries and the optimized Fe–C, Fe–S distances are in reasonable agreement with the EXAFS data (Table 3). However, while the Fe–Fe distance in the -equatorial conformer (Fig. 4C) is 2.51 Å and agrees well with the experimental value of 2.49 Å, the Fe–Fe distance of the -axial-conformer is 2.57 Å and does not match the EXAFS data. Additionally, the -axial conformer (Fig. 4B) leads to a  $\mu\text{-CO}$  ligand with  $\nu_{\text{CO}}$  at 1840  $\text{cm}^{-1}$  (Table 3) which is not consistent

Table 1 Experimental Mössbauer parameters obtained from the experiments at 90 K

Mössbauer parameters	$\text{Fe}_2\text{S}_2(\text{CO})_6(\text{CH}_2)_2\text{NPhBr}$	Complex <b>1</b>
$\delta_{\text{iso}}$ ( $\text{mm s}^{-1}$ )	$-0.051 \pm 0.003$	$0.05 \pm 0.01$
$\Delta E_{\text{Q}}$ ( $\text{mm s}^{-1}$ )	$0.846 \pm 0.001$	$0.85 \pm 0.01$



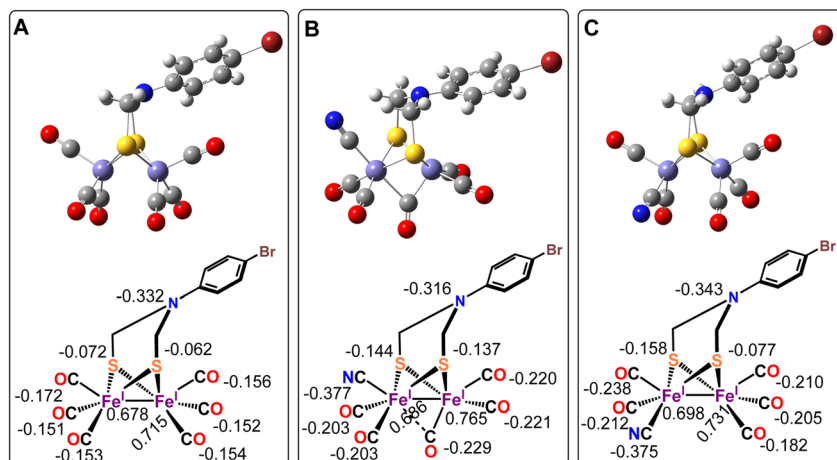


Fig. 4 Optimized geometries of  $p\text{-BrC}_6\text{H}_4\text{N}(\text{CH}_2\text{S})_2\text{Fe}_2\text{CO}_6$  complex (A, top) and complex 1 in axial- $\text{CN}^-$  (B, top) & equatorial- $\text{CN}^-$  (C, top) form. The calculated Mulliken charges are mentioned with chem draws of the respective figures at bottom.

Table 3 Computationally determined structural and spectroscopic parameters for axial- $\text{CN}^-$  and equatorial- $\text{CN}^-$  geometrical conformers of complex 1 and the experimentally obtained values

Structure	Bond length (Å)				IR stretching ( $\text{cm}^{-1}$ )	
	Fe–CO	Fe–CN	Fe–Fe	Fe–S	$\nu_{\text{CO}}$	$\nu_{\text{CN}}$
axial- $\text{CN}^-$ (4B)	1.74 (CO <sub>t</sub> ) 1.80, 2.11 (CO <sub>b</sub> )	1.90	2.57	2.35	1840, 1934, 1965, 1979, 2015	2102
Equatorial- $\text{CN}^-$ (4C)	1.74	1.90	2.51	2.29	1928, 1946, 1962, 1978, 2020	2114
1 <sup>a</sup>	1.74 <sup>b</sup>	1.88 <sup>b</sup>	2.49 <sup>b</sup>	2.28 <sup>b</sup>	1922 <sup>c</sup> , 1950 <sup>c</sup> , 1960 <sup>c</sup> , 1982 <sup>c</sup> , 2033 <sup>c</sup>	2093 <sup>c</sup>
$p\text{-BrC}_6\text{H}_4\text{N}(\text{CH}_2\text{S})_2\text{Fe}_2\text{CO}_6$ (4A)	1.79 <sup>d</sup>	NA	2.50 <sup>d</sup>	2.26 <sup>d</sup>	1999 <sup>c</sup> , 2038 <sup>c</sup> , 2076 <sup>c</sup>	NA
	1.77	NA	2.48	2.29	2005, 2032, 2066	

<sup>a</sup> The synthesized complex 1. <sup>b</sup> Values were obtained from EXAFS data. <sup>c</sup> Experimentally obtained IR stretching frequencies in  $\text{CH}_3\text{CN}$  solution.

<sup>d</sup> Values were obtained from XRD data.

with the experimentally observed spectrum of complex 1 (Fig. 1A, red). Thus, based on the concurrence between the experimental data and the DFT calculated structure and vibrational properties we conclude that the -equatorial conformer of complex 1 (Fig. 4C) is the dominating species in solution.

The calculated Mulliken charges indicate that the -CO ligands in the precursor  $\text{Fe}_2\text{S}_2(\text{CO})_6(\text{CH}_2)_2\text{NPhBr}$  complex (Fig. 4A) bears overall negative charge suggesting that there is significant back bonding from the occupied orbitals into the unoccupied CO  $\pi^*$  orbitals. On - $\text{CN}^-$  incorporation (*i.e.* -axial- and equatorial- $\text{CN}^-$ ) the amount of negative charge delocalized into the -CO ligands increase. This implies stronger back donation into the -CO  $\pi^*$  orbitals when  $\text{CN}^-$  ligand is introduced. The total charge on the  $\text{CN}^-$  ligand is -0.377 and -0.375 for -axial- and -equatorial- $\text{CN}^-$ , respectively, indicating that most of the negative charge of the  $\text{CN}^-$  ligand is shifted into the cluster; mostly into the -CO ligands (Fig. 4B and C) as suggested by lowering of  $\nu_{\text{CO}}$  vibrations in complex 1 relative to the precursor complex observed experimentally (Fig. 1A). Note that the Mulliken charge on the bridgehead N atom remains unaltered.

## Electrocatalytic reduction of proton in aqueous medium under heterogeneous conditions on EPG

**Electrocatalytic  $\text{H}_2$  evolution (HER) under heterogeneous condition.** The electrode for heterogeneous electrochemical investigations was prepared by drop casting complex 1 on edge plane graphite (EPG) electrode. XPS data of the modified EPG surface showed Fe 2p<sub>3/2</sub> and 2p<sub>1/2</sub> transitions (Fig. S2†) at 710.9 eV and 724.5 eV, respectively. These values are typical for binuclear  $[\text{Fe}_2\text{S}_2]\text{-H}_2\text{ase}$  models.<sup>70</sup> The nitrogen 1s region (Fig. S2†) showed three components at 397.7 eV, 399.2 eV and 400.5 eV corresponding to the cyanide, amine and the tetraalkylammonium counter cation, respectively.<sup>89</sup> Presence of thiolate sulphur is evidenced by the S 2p at 163–164 eV (Fig. S2†).

In aqueous solvent CV data indicate that the reduction of complex 1, upon immobilization onto EPG electrode, is observed at -0.35 V vs. NHE (Fig. 5A, red dashed line). This redox event is attributed to the  $\text{Fe}(\text{I})\text{-Fe}(\text{I})/\text{Fe}(\text{I})\text{-Fe}(\text{0})$  process and the area under the CV response indicate  $2.25 \pm 0.25 \times 10^{-12} \text{ mol cm}^{-2}$  electrochemically active complex 1 present on the EPG. Note that while the  $\text{Fe}(\text{I})\text{-Fe}(\text{I})/\text{Fe}(\text{I})\text{-Fe}(\text{0})$  is -0.76 V in an organic solvent like  $\text{CH}_3\text{CN}$  (Fig. 5A, red), it is demonstrated to shift to considerable higher potentials at -0.35 V vs. NHE (Fig. 5A, dashed red) in aqueous medium due to enhanced

solvation of the negatively charged species produced upon reduction by water as was observed for the precursor complex.<sup>70,90</sup> Electrocatalytic hydrogen evolution (HER) by immobilized **1** was investigated in aq. H<sub>2</sub>SO<sub>4</sub> solution by linear sweep voltammetry (LSV). Subsequently, rotating ring disk electrochemistry (RRDE) set up fitted with a Pt-ring encircling the working EPG electrode allowed us *in situ* detection of the hydrogen,<sup>91</sup> produced by the working electrode on sweeping from positive to negative potential. In 0.002 N H<sub>2</sub>SO<sub>4</sub> (pH ~2.7) solutions, scanning from 0.2 V to -0.8 V with scan rate 50 mV s<sup>-1</sup> at 300 rpm rotation speed, a large catalytic current was observed with an onset at -0.3 V (*I*<sub>cat</sub> = 100 μA) and it reached to a maximum value at -0.65 V (Fig. 5B, red). The hydrogen production was concomitantly detected by the Pt-ring, held at a constant potential 0.7 V where it re-oxidized the H<sub>2</sub>, produced by the working electrode and radially diffuses out to this encircling Pt ring, to H<sup>+</sup> generating an oxidation current (Fig. 5B, red dashed line).<sup>91</sup> No such catalytic current was observed on a bare EPG electrode under identical condition (Fig. 5B, purple). This indicates electrocatalytic hydrogen production by complex **1**. For further confirmation, controlled potential electrolysis (CPE) was performed at -0.4 V vs. NHE in a gas tight two compartment water jacketed cell and the produced gases were characterized by the head space analysis of the cathodic compartment in gas chromatography fitted with thermal conductivity detector (GC-TCD) where H<sub>2</sub> was identified (Fig. 5B, inset, green trace). The HER activity of **1** was compared

with its precursor complex *p*-BrC<sub>6</sub>H<sub>4</sub>N(CH<sub>2</sub>S)<sub>2</sub>Fe<sub>2</sub>CO<sub>6</sub> *i.e.*, without a CN<sup>-</sup> ligand. The LSV data (Fig. 5C, red) indicate that **1** catalyses HER with 350 mV lower onset potential than the precursor complex in 0.002 N H<sub>2</sub>SO<sub>4</sub> solution (Fig. 5C, olive green). This is because while **1** catalyses HER from its Fe(I)-Fe(0) state, the precursor *p*-BrC<sub>6</sub>H<sub>4</sub>N(CH<sub>2</sub>S)<sub>2</sub>Fe<sub>2</sub>CO<sub>6</sub> complex catalyzes HER from its Fe(0)-Fe(0) state. Thus, inclusion of CN<sup>-</sup> leads to higher p*K*<sub>a</sub> of the cluster such that the one electron reduced Fe(I)-Fe(0) state can be protonated and reduction to the two electron reduced Fe(0)-Fe(0) state can be avoided.

To characterize the catalytic ability of complex **1** turn over number (TON), turn over frequency (TOF), faradaic yield (FY) and overpotential (η) of HER are determined. The FY for HER was determined by performing controlled potential electrolysis (CPE) at -0.4 V vs. NHE in 0.1 N H<sub>2</sub>SO<sub>4</sub> (Fig. S6A, red†). Over a period of 1 hour, 9.43 C charge had been dispensed from the electrode (*i.e.*, 9.7 × 10<sup>-5</sup> moles) and concurrently ~1 ml H<sub>2</sub> gas was evolved during CPE. From these results, the FY is determined to be 92 ± 7%. No significant current was observed when bare EPG disc was tested under similar conditions (Fig. S6A,† green). Thus, the TON calculated for this catalyst during CPE is > 10<sup>7</sup> and the average TOF is ~2230 s<sup>-1</sup> at pH 1. This is very close to the value of ~4000 s<sup>-1</sup> determined from *I*<sub>cat</sub>/[τ] (ratio of catalytic current and CV current) experiments in 0.1 N of [H<sup>+</sup>] (Fig. 6A). The η of HER is determined from LSV data at 0.002 N [H<sup>+</sup>]. The standard potential for H<sub>2</sub>/H<sup>+</sup> couple at this proton concentration is -0.16 V whereas onset of HER (*I*<sub>cat</sub> = 100 μA,

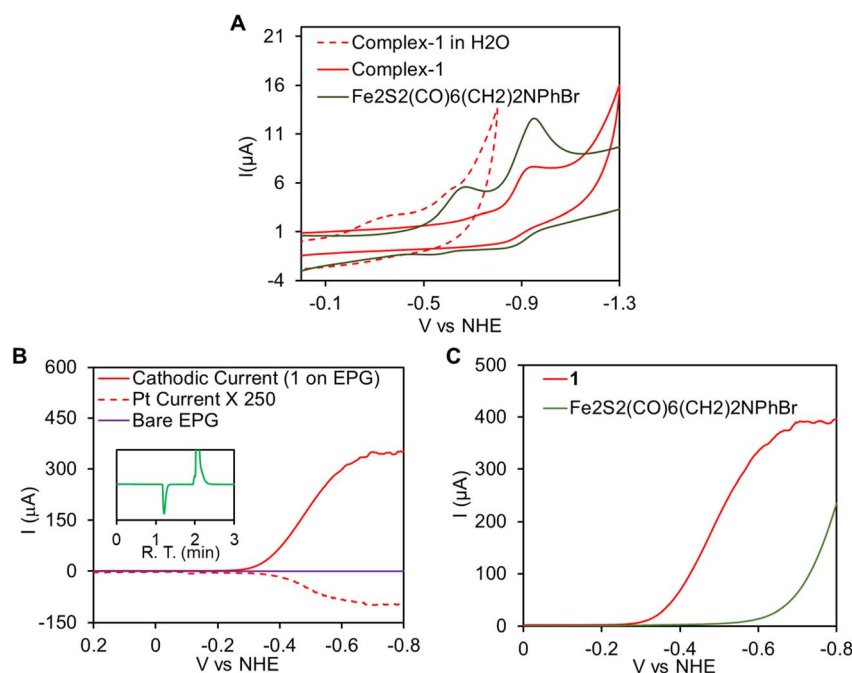


**Fig. 5** (A) Overlay of the CV traces of complex **1** (red) and its precursor *p*-BrC<sub>6</sub>H<sub>4</sub>N(CH<sub>2</sub>S)<sub>2</sub>Fe<sub>2</sub>CO<sub>6</sub> complex in acetonitrile medium (olive green) under homogeneous conditions. The CV of complex **1** immobilized on EPG in aqueous medium is shown in red dashed line. (B) RRDE with complex **1** immobilized on EPG working electrode (red line, indicating electrocatalytic H<sup>+</sup> reduction) which is swept from 0.2 V to -0.8 V and the corresponding Pt-ring current (red dashed line, indicating H<sub>2</sub> oxidation *i.e.*, detection) with the ring held at a constant potential of 0.7 V in aqueous 0.002 N H<sub>2</sub>SO<sub>4</sub>. Bare EPG trace is shown in purple, inset gas chromatogram of the headspace gas analysis after CPE of complex **1** immobilized on EPG at -0.4 V vs. NHE in 0.1 N H<sub>2</sub>SO<sub>4</sub>. (C) Overlay of the LSV traces for complex **1** (red) and *p*-BrC<sub>6</sub>H<sub>4</sub>N(CH<sub>2</sub>S)<sub>2</sub>Fe<sub>2</sub>CO<sub>6</sub> (Olive green) on EPG.



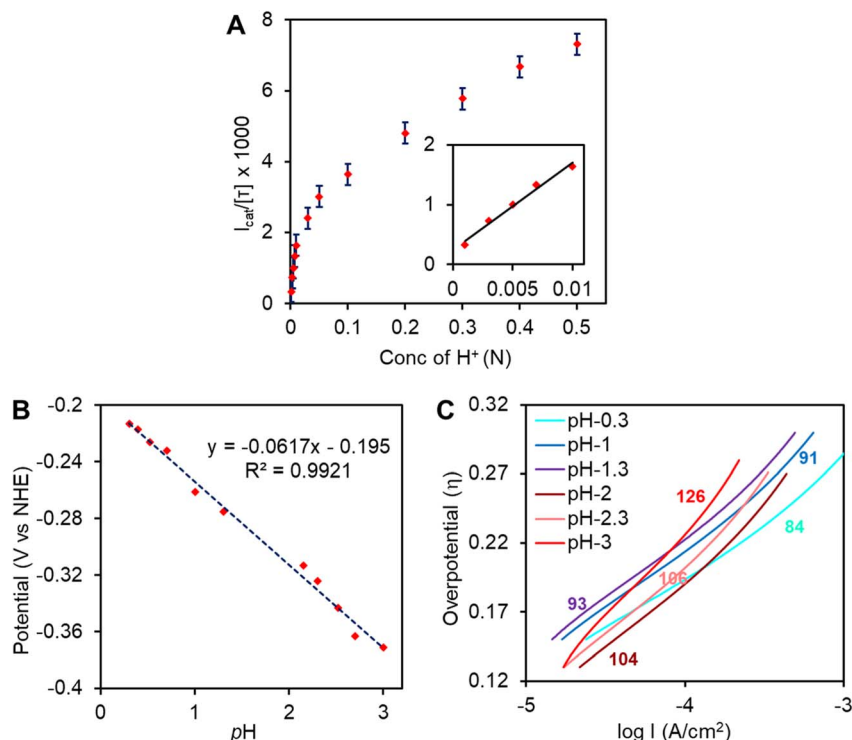


Fig. 6 (A) Plot of  $I_{\text{cat}}/[\tau]$  at varying acid concentrations of complex **1** on EPG.  $I_{\text{cat}}$  values were recorded at  $-0.5$  V vs. NHE for each  $[\text{H}^+]$ , inset plot of  $I_{\text{cat}}/[\tau]$  at lower acid concentrations. (B) Onset potential (V vs. NHE) @  $I_{\text{cat}} = 100 \mu\text{A}$  vs. pH plot. (C) Tafel plots at different pHs. The values are the Tafel slopes at different pHs and reported in  $\text{mV dec}^{-1}$ .

area of electrode  $\sim 0.1 \text{ cm}^2$  i.e.  $j_{\text{cat}} = 1 \text{ mA cm}^{-2}$  where  $j$  is the exchange current density) is  $-0.4$  V. Hence, the onset overpotential is only about  $0.24$  V, which is one of the lowest overpotential for HER to be reported so far for any  $[\text{Fe}-\text{Fe}]$   $\text{H}_2\text{ase}$  inspired molecular catalyst in aqueous medium. The XPS data (Fig. S2†) and the ATR-IR (Fig. S6B†) data of the graphite electrode were collected after CPE and showed that the catalyst was stable over the CPE time scale. This is also implied by the constant slope of the current during CPE.

### Mechanistic considerations

**Effect of acid concentrations.** By varying bulk  $\text{H}^+$  concentration over a range of  $0.001 \text{ N}$ – $0.5 \text{ N}$   $[\text{H}^+]$  (pH 3–pH 0.3), a sharp increase of the catalytic current was observed (Fig. S3†) and reached to a maximum  $I_{\text{cat}}/[\tau]$  value (i.e., TOF) of  $7300 \text{ s}^{-1}$  at  $0.5 \text{ N H}_2\text{SO}_4$  (Fig. 6A). The saturation of  $I_{\text{cat}}$  at high acid concentration may not reflect saturation of catalytic activity as the catalysis is retarded by bubble accumulation ( $\text{H}_2$  gas, Fig. S9†) on the rotating electrode (even at  $2000 \text{ rpm}$  rotation rate) at high proton concentrations. This  $7300 \text{ s}^{-1}$  TOF value remains almost unchanged over consecutive 50 scans at  $0.5 \text{ N H}_2\text{SO}_4$  (Fig. S4†). At lower acid concentrations (Fig. 6A, inset), where bubbles do not accumulate on the rotating electrode, the  $I_{\text{cat}}/[\tau]$  value linearly increased with the  $[\text{H}^+]$ , indicating pseudo 1st order kinetics of HER. Note that the  $(i_{\text{cat}}/\tau)$  of the hydrogen production  $\sim 300 \text{ s}^{-1}$  at  $0.001 \text{ N H}_2\text{SO}_4$  i.e., at pH = 3. The onset potential ( $I_{\text{cat}} = 100 \mu\text{A}$ ) for the faradaic current showed a positive shift with a slope of  $60$

$\pm 2 \text{ mV}$  per unit change in pH of the solution (Fig. 6B). These two observations suggest  $1\text{e}^-/1\text{H}^+$  proton coupled electron transfer is involved in rate determining step. Further analysis of the LSV currents at low current range showed different slopes in  $\log I$  vs.  $\eta$  plots (Tafel plot) at different pHs (Fig. 6C). At higher pHs, a slope of  $126 \text{ mV dec}^{-1}$  was obtained while a gradual decrease of the slope up to  $84 \text{ mV dec}^{-1}$  was attained at lower pHs (pH = 0.3). The decrease in slope value can be attributed to bubble formation encountered or some side reaction at higher acid concentrations. Notably, a  $120 \text{ mV dec}^{-1}$  slope is expected for a metal-hydride formation rate determining step according to pure Volmer kinetic mechanism.<sup>92–94</sup> Overall a PCET step for di-iron hydride,  $[\text{Fe}(\text{I})-\text{Fe}(\text{II})]-\text{H}$ , formation is proposed as rate determining step for this catalysis by complex **1**. Unfortunately, no evidence for the formation of this species during heterogeneous catalysis on the EPG electrode can be provided but evidence for the formation of this species is provided using FTIR-SEC under homogeneous conditions (*vide infra*).

### Kinetic analyses

**Koutecky–Levich analysis.** Complex **1** reduces  $\text{H}^+$  at diffusion-controlled limit at low  $[\text{H}^+]$  with overpotential of  $0.24$  V. The diffusion limited current has two components–

$$I_{\text{cat}}^{-1} = i_{\text{K}}(E)^{-1} + i_{\text{L}}^{-1}$$

Where  $i_{\text{K}}(E)$  is the potential dependent kinetic current and  $i_{\text{L}}$  is the Levich current which is given by,

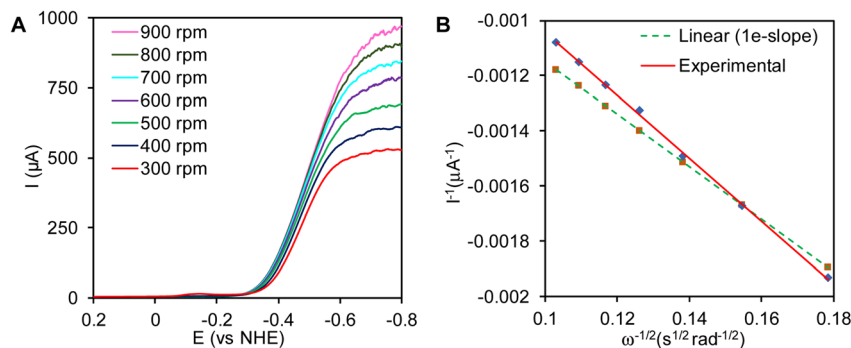


Fig. 7 (A) Plot of linear sweep voltammetry (LSV) with increasing rotation rates scanning from 0.2 V to  $-0.8$  V in  $0.005$  N  $\text{H}_2\text{SO}_4$  solution. (B) Plot of the  $(1/I_{\text{cat}})$  vs.  $1/\omega^{1/2}$  where catalytic current ( $I_{\text{cat}}$ ) measured at  $-0.6$  V.

$$i_L = 0.62nFA[\text{H}^+](D_{\text{H}^+})^{2/3}\omega^{1/2}\nu^{-1/6}$$

where  $n$  is the number of electrons transferred to the substrate,  $A$  is the area of the disc ( $0.096 \text{ cm}^2$ ),  $[\text{H}^+]$  is the concentration of  $\text{H}^+$  *i.e.*,  $0.005$  N,  $D_{\text{H}^+}$  is the diffusion coefficient of  $\text{H}^+$  ( $9.3 \times 10^{-5} \text{ cm}^2 \text{ s}^{-1}$ ),  $\omega$  is the angular velocity of the disc and  $\nu$  is the kinematic viscosity of the solution ( $0.01 \text{ cm}^2 \text{ s}^{-1}$ ).

The plot of inverse of catalytic current, at  $-0.6$  V vs. NHE where the current is mass transfer controlled, varied linearly with the inverse of the square root of the angular rotation rates (Fig. 7A). The plot of  $I^{-1}$  vs.  $\omega^{-1/2}$  was linear and the slope obtained from the experimental results was similar to the predicted slope for  $1e^-$  reduction process (Fig. 7B). This indicates that complex **1** reduces the  $\text{H}^+$ , by one electron to  $1/2 \text{ H}_2$ , *i.e.*,  $\text{H}^+ + e^- \rightarrow 1/2 \text{ H}_2$ .

The potential dependent current  $i_K(E)$  is obtained from the inverse of the intercept of the K-L plot and is expressed as,

$$I_K(E) = k[\text{H}^+]nF[A][\tau][\text{H}^+]$$

where  $k_{[\text{H}^+]}$  is the 2nd order rate constant for  $\text{H}^+$  reduction,  $[\tau]$  is the number of molecules of **1** on the electrode,  $A$  is the macroscopic area of the electrode and  $n$ ,  $F$  and  $[\text{H}^+]$  has their usual meanings. The second order rate of proton reduction has been calculated to be  $\sim 2.5 \pm 0.2 \times 10^{11} \text{ M}^{-1} \text{ s}^{-1}$ .

In the absence of *in situ* spectroscopic methods amenable to probe a catalyst heterogenized on graphite electrodes in *operando*, HER in organic solvents was investigated with the goal of identifying potential intermediates involved in HER using IR-SEC.

**CV under homogenous condition.** Cyclic voltammetry (CV) of a solution of complex **1** in  $\text{CH}_3\text{CN}$  showed a peak ( $E_{\text{red}}$ ) centred at  $-0.76$  V with peak-to-peak separation ( $\Delta E_p$ ) of  $120$  mV (Fig. 5A, red). This represents the reduction of the  $\text{Fe(II)}-\text{Fe(II)}$  state to the  $\text{Fe(II)}-\text{Fe(0)}$  state as demonstrated for similar synthetic models.<sup>95</sup> The  $\text{Fe(II)}-\text{Fe(II)}/\text{Fe(II)}-\text{Fe(0)}$  process is lowered by  $140$  mV relative to that of the precursor  $p\text{-BrC}_6\text{H}_4\text{N}(\text{CH}_2\text{S})_2\text{-Fe}_2\text{CO}_6$  complex due to ligation of an anionic  $\text{CN}^-$  ligand.

A catalytic current at similar potential was observed (Fig. 8A, blue line) in the presence of 2 equivalents of *p*-toluenesulfonic acid (*p*TsOH,  $\text{p}K_a \approx 8.3$  in  $\text{CH}_3\text{CN}$ )<sup>96</sup> and the catalytic current increases significantly with sequential addition of *p*TsOH. The sharp increase in its current intensity indicates that complex **1** has the ability for the electrocatalytic reduction of protons to  $\text{H}_2$ . To confirm this controlled potential electrolysis (CPE) was performed at  $-0.9$  V vs. NHE of the  $0.3$  mM acetonitrile solution of complex **1** in the presence of 80 equivalent of *p*-toluenesulfonic acid (*p*TsOH) (Fig. 9A). The headspace gas analysis by GC-TCD confirmed the produced gas to be  $\text{H}_2$  (Fig. 8B, red

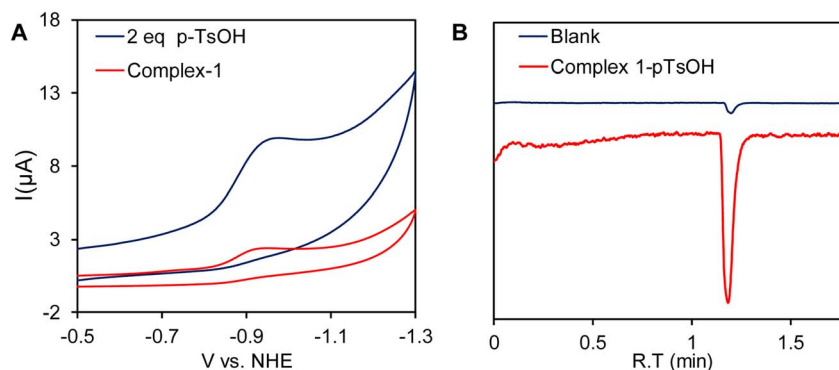


Fig. 8 (A) Cyclic voltammogram of complex **1** in  $\text{CH}_3\text{CN}$  (red line) and in the presence of *p*-toluenesulfonic acid (*p*TsOH) (blue line) under homogeneous conditions. (B) Gas chromatogram of the headspace gas analysis after CPE of complex **1** in the presence of 80 equivalent of *p*-TsOH in  $\text{CH}_3\text{CN}$  medium (red trace). The experiment was also repeated with blank electrodes under similar conditions (blue trace).





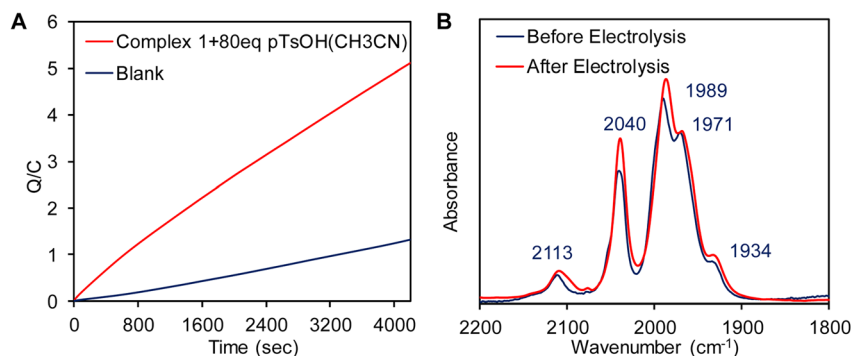


Fig. 9 (A) Overlay of controlled potential bulk electrolysis with the complex 1 at  $-0.9$  V vs. NHE in  $\text{CH}_3\text{CN}$  medium in the presence of 80 equivalent of  $p\text{TsOH}$  (red line) and without complex 1 (blue line) under identical conditions. (B) FT-IR of the of complex 1 before and after bulk electrolysis in the presence of  $p\text{TsOH}$ .

trace). During the CPE 5.12 C charge was consumed over the course of 70 min (Fig. 9A) and 0.5 ml of  $\text{H}_2$  was evolved. From these results, the FY was determined to be 84% and the TON was calculated to be 15. In the absence of the catalyst no significant amount of  $\text{H}_2$  was produced under similar condition (Fig. 8B, blue trace). The FTIR spectra recorded before and after the CPE experiment confirmed that the catalyst is stable and also the  $\text{CN}^-$  ligands are not protonated under these conditions as has been reported for di-cyano complexes (Fig. 9B).<sup>34</sup>

**FTIR-SEC.** The resting state of complex 1 is likely a *trans*- $\text{Fe}(\text{I})-\text{Fe}(\text{I})$  configuration; a conclusion drawn from the agreement of its vibrational frequencies to those obtained through DFT calculations (Table 4) and EXAFS data (Table 3). Upon the addition of 1 equivalent *p*-toluenesulfonic acid ( $p\text{TsOH}$ ), notable changes were observed in the vibrational spectra of complex 1. Specifically, all frequencies associated with carbonyl and cyanide groups were blue shifted to higher wavenumbers by  $\approx 10\text{--}20\text{ cm}^{-1}$  (Fig. 11A, blue line). Based on previous reports we can conclude that the magnitude of the shift is similar to the result observed upon protonation of neutral -ADT bridged complex with strong acid and characteristic for protonation of the bridgehead nitrogen (Fig. 11A).<sup>97,98</sup> Thus, the  $\text{CN}^-$  ligand is not protonated in the presence of  $p\text{TsOH}$  and this is likely because of the delocalization of the electron density of the  $\text{CN}^-$  into the cluster as indicated by FTIR data and DFT calculations of this complex. DFT calculations also support the observed blue shift in the  $\nu_{\text{CO}}$  vibrations (Fig. 11C and Table 4). To further probe and characterize the intermediates that arise during the catalytic cycle, we conducted FTIR spectro-electrochemistry (IR-

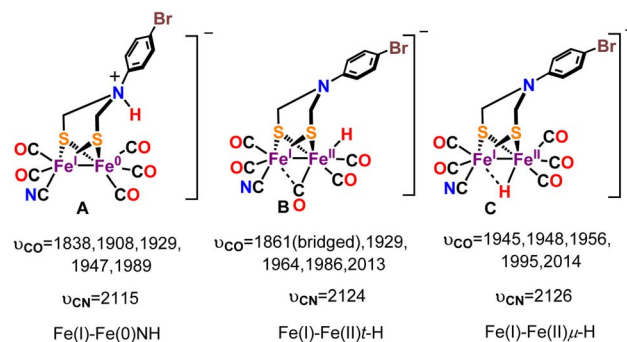


Fig. 10 Probable one electron reduced protonated species and their computed  $\nu_{\text{CO}}$  and  $\nu_{\text{CN}}$  vibrational frequencies.

SEC) experiment. We subjected the N-protonated form of complex 1 (Complex 1 + 1 eq.  $p\text{TsOH}$ ) to electrochemical reduction by performing controlled potential electrochemistry (CPE) at  $-0.9$  V vs. NHE, within a conventional OTTLE cell to probe the mechanism of HER.

Reduction of complex 1 in the presence of 1 equivalent  $p\text{TsOH}$  did not result in red shift in the  $\nu_{\text{CO}}$  and  $\nu_{\text{CN}}$  vibrations (Fig. 11B, blue line) as would be expected for a reduction event in the cluster which would have increased back bonding to carbonyl and cyanide ligands. For example, reduction of the  $\text{Fe}(\text{I})-\text{Fe}(\text{I})$  of a ADT bound  $\text{Fe}_2(\text{CO})_6$  cluster accompanied with protonation of the ADT nitrogen is associated with  $>100\text{ cm}^{-1}$  red shift in the  $\nu_{\text{CO}}$ .<sup>99</sup> Specifically, one of the  $\nu_{\text{CO}}$  vibrations red shifted significantly to  $1876\text{ cm}^{-1}$  which is much lower than the

Table 4 Experimental and theoretical vibrational frequencies of different species involved in catalytic cycle

Complex	IR stretching frequencies ( $\text{cm}^{-1}$ )			
	Experimental (In $\text{CH}_3\text{CN}$ )		Theoretical (BP86)	
	$\nu_{\text{CN}}$	$\nu_{\text{CO}}$	$\nu_{\text{CN}}$	$\nu_{\text{CO}}$
Complex 1 [ $\text{Fe}(\text{I})-\text{Fe}(\text{I})$ ]	2093	2033, 1982, 1960, 1950, 1922	2114	2020, 1978, 1962, 1946, 1928
Complex 1 + $p\text{TsOH}$ [ $\text{Fe}(\text{I})-\text{Fe}(\text{I})\text{NH}^+$ ]	2113	2040, 1989, 1971, 1961, 1934	2127	2042, 2009, 1989, 1962, 1955
Complex 1 + $p\text{TsOH} + (\text{e}^-)$ [ $\text{Fe}(\text{I})-\text{Fe}(\text{II})\text{t-H}$ ]	2095	2036, 1976, 1950, 1923, 1876	2124	2013, 1986, 1964, 1929, 1861
Complex 1 + $p\text{TsOD} + (\text{e}^-)$ [ $\text{Fe}(\text{I})-\text{Fe}(\text{II})\text{t-D}$ ]	2095	2036, 1974, 1950, 1925, 1860	2124	2013, 1986, 1964, 1929, 1852

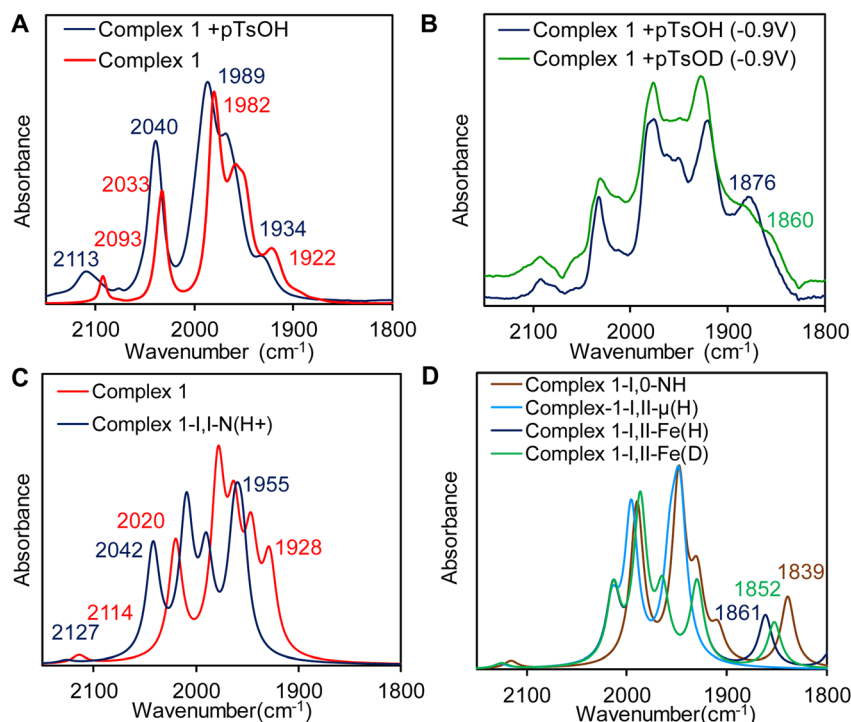


Fig. 11 (A) FTIR spectra of complex 1 (red line) and complex 1 in the presence of 1 equivalent *p*TsOH (blue line). (B) IR-SEC data of complex 1 @  $-0.9$  V vs. NHE in the presence of *p*TsOH (blue line) and *p*TsOD (green line). (C) Computed vibrations of complex 1 (red line) and complex 1 in the presence of 1 equivalent of *p*TsOH (blue line) and *p*TsOD (green line). (D) Computed vibrations of model A (orange line), B (dark blue line) and C (blue line) (Fig. 10) and the deuterated form of model B (green line).

other terminal  $\nu_{\text{CO}}$  vibrations and would be consistent with a  $\mu\text{CO}$  formation during reduction in the presence of  $\text{H}^+$  source. Furthermore, the peak at  $1876\text{ cm}^{-1}$  (Fig. 11B, blue line) appears to shift to  $1860\text{ cm}^{-1}$  (Fig. 11B, green line) when *p*TsOD was used as a  $\text{D}^+$  source *i.e.*, this  $\nu_{\text{CO}}$  shows a H/D isotope effect. Note that a Fe–H vibration is expected to show a H/D isotope shift  $>570\text{ cm}^{-1}$  using simple harmonic oscillator approximation. Similarly, H/D shifts associated with hydrogen bonding to  $-\text{CO}$  ligands are very small.<sup>100</sup> The shift observed here is  $16\text{ cm}^{-1}$  which suggests that the species produced in IR-SEC is likely to be a metal hydride species where a  $\nu_{\text{CO}}$  coupled to a  $\nu_{\text{Fe-H}}$ . Similar shift of a  $\mu\text{-CO}$  due to coupling with a terminal hydride trans to it in  $[\text{Fe-Fe}] \text{H}_2\text{ases}$ .<sup>27</sup> There is some residual  $1876\text{ cm}^{-1}$  peak in the deuterated solvent from residual  $\text{H}_2\text{O}$  in the electrolyte.

#### DFT calculations on possible structure of the intermediate.

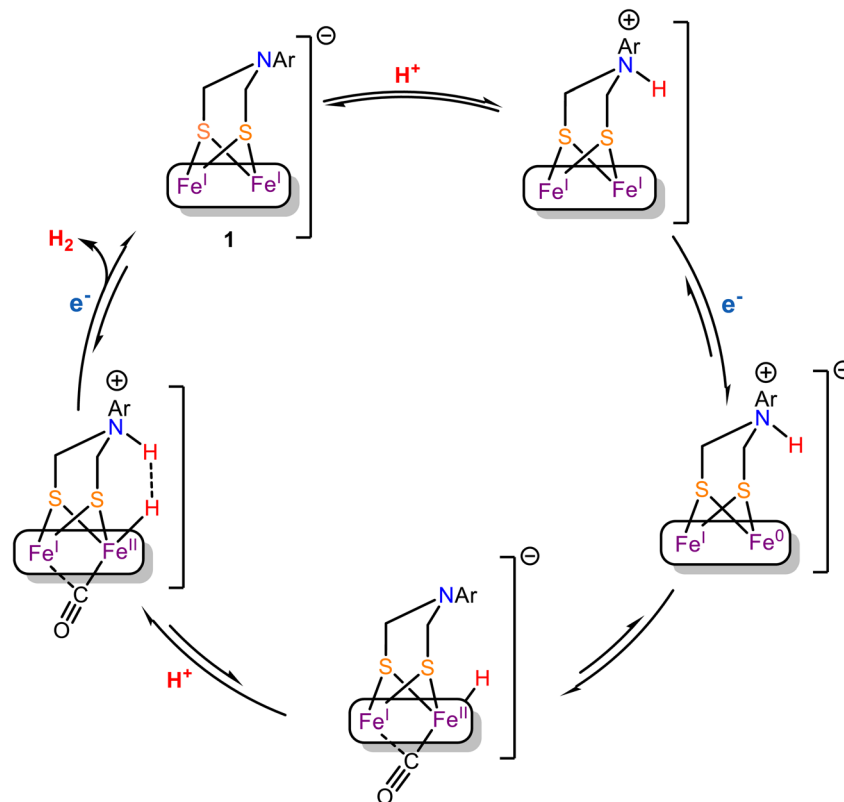
DFT calculations provided a valuable insight into the nature of this one electron reduced protonated species. Three different one electron reduced protonated species may be formed during the catalytic cycle. They include models with ADT protonated and cluster reduced for  $\text{Fe(I)-Fe(0)}$  state (Fig. 10A,  $\text{Fe(I)-Fe(0)NH}$ ), a model which is reduced by one electron and protonated at the Fe to result in a *t*-H (Fig. 10B,  $\text{Fe(I)-Fe(II)t-H}$ ), a model which is reduced by one electron and protonated to result in a  $\mu\text{-H}$  (Fig. 10C,  $\text{Fe(I)-Fe(II)}\mu\text{-H}$ ) and their computed  $-\nu_{\text{CO}}$  and  $-\nu_{\text{CN}}$  vibrational stretching frequencies are also indicated. Note that only the equatorial conformation is considered in these calculations. The experimental vibrations match well with computed

vibrations of the  $\text{Fe(I)-Fe(II)t-H}$  species, containing a terminal hydride (*t*-H, Fig. 11B and D). One of the  $-\text{CO}$  moves to a semi-bridging position (*i.e.*,  $\mu\text{-CO}$ ) resulting in a substantial weakening of its  $\mu\text{-CO}$  relative to those of the terminal  $\text{CO}$ 's. This  $\mu\text{-CO}$  is trans to the *t*-H (Fig. 10B) resulting in mixing of the  $\nu_{\text{CO}}$  and  $\nu_{\text{Fe-H}}$  which results in the shift of the  $\nu_{\text{CO}}$  at  $1861\text{ cm}^{-1}$  to  $1852\text{ cm}^{-1}$  when the *t*-H is replaced by *t*-D in these calculations (Fig. 11C). The  $\text{Fe(I)-Fe(II)}\mu\text{-H}$  model (Fig. 10C) which does not have a  $\mu\text{-CO}$  cannot explain the weak  $\nu_{\text{CO}}$  observed at  $1876\text{ cm}^{-1}$  and the  $\text{Fe(I)-Fe(0)NH}$  model (Fig. 10A) does not couple to  $\nu_{\text{CO}}$  and hence does not show a H/D effect on it as observed. Thus, the computed models bearing the  $\mu\text{-H}$  and *NH* do not show any H/D isotope sensitive vibration in this region. The computed vibrations for doubly protonated species blue shift significantly from the experimental data and were eliminated from consideration (Fig. S7 and S8B†). The results obtained from the IR-SEC and DFT calculation suggest that (a) the reduced species bears a  $\mu\text{-CO}$  ligand and (b) the proton vibration is involved in the  $1876\text{ cm}^{-1}$   $\nu_{\text{CO}}$  mode which is likely to occur is the hydride is trans to the  $\mu\text{-CO}$  ligand. The H/D isotopic shift of this  $1876\text{ cm}^{-1}$  vibration observed experimentally which is also present in the computational model supports this proposal.

## Discussion

The EXAFS, Mössbauer and FTIR data of complex 1 is consistent with the presence of terminal cyanide ligand. Thus, along with the  $\mu\text{-ADT}$  and the terminal  $\text{CN}^-$  ligand, this model is a close





Scheme 3 Proposed mechanistic pathway for HER catalyzed by complex 1.

structural analogue of the active site of the  $[\text{Fe}-\text{Fe}]$   $\text{H}_2$ ases. The presence of the  $\text{CN}^-$  raises the basicity of the cluster in **1** such that HER current of the  $\text{CN}^-$  bound form at higher pH's remarkably higher relative to the precursor complex. Under aqueous conditions, the 1st order dependence of the rate with  $[\text{H}^+]$  at low acid concentrations suggest that binding of  $\text{H}^+$  is involved in rate determining step (rds). The 62 mV/pH slope of the pH vs. onset potential plot (Fig. 6B) suggest that proton coupled electron transfer (PCET) is operating at the potential determining step in the kinetic region.<sup>101,102</sup> Now, protonation could occur either at the bridgehead N to generate reduced N-protonated species or at the reduced Fe-centre to form a Fe-H species (terminal or bridging).<sup>103</sup> The Tafel slope is determined to be  $126 \text{ mV dec}^{-1}$  which is close to the value expected for Volmer mechanism implying the involvement of a Fe-H species in the rds.<sup>92-94</sup> In an organic solvent ( $\text{CH}_3\text{CN}$ ), under homogeneous conditions, complex **1** catalyze HER at  $-0.9 \text{ V vs. NHE}$  (Fig. 8A) and remains stable during CPE for more than an hour (Fig. 9). *In situ* FTIR-SEC provide preliminary evidence for a terminal hydride  $[\text{Fe}(\text{I})-\text{Fe}(\text{II})-\text{H}]$  with a  $\mu\text{-CO}$  during catalysis when the  $\nu_{\text{CO}}$  shifts on deuteration due to coupling with a t-H in a fashion similar to that observed for  $[\text{Fe}-\text{Fe}]$   $\text{H}_2$ ase.<sup>27</sup> The accumulation of the hydride species during HER in organic medium implies that its further protonation is likely the rds which is in line with the suggestions from Tafel slope obtained under aqueous conditions. However, the solvation energies of species involved in catalysis will be very different in aqueous and organic solvents and the mechanism may vary. To rationalize the sequence of

events, we proposed that the mechanistic pathway proposed by Rauchfuss is at play here (Scheme 3) *i.e.* (i) In the presence of  $p\text{TsOH}$ , the complex **1** forms a N-protonated complex, (ii) the N-protonated complex **1** undergoes a one-electron reduction under electrochemical condition along with an intramolecular proton transfer from the bridge head nitrogen atom to the reduced  $\text{Fe}(\text{I})-\text{Fe}(\text{0})$  center to form the  $-\text{CO}$  bridged  $\text{Fe}(\text{I})-\text{Fe}(\text{II})-\text{H}$  species. This step may be mediated by  $\text{Fe}(\text{I})-\text{Fe}(\text{0})\text{NH}$  species but the isomerization of it to  $\text{Fe}(\text{I})-\text{Fe}(\text{II})-\text{H}$  may be too rapid to be observed in IR-SEC. (iii) The protonation of the  $[\text{Fe}(\text{I})-\text{Fe}(\text{II})-\text{H}]$  species in the rds then leads to  $\text{H}_2$  evolution.

The  $\text{CN}^-$  bound complex **1** exhibits the  $\text{Fe}(\text{I})-\text{Fe}(\text{I})/\text{Fe}(\text{I})-\text{Fe}(\text{0})$   $E_{1/2}$  at  $-0.76 \text{ V}$  in acetonitrile which is 140 mV more cathodic than the  $E_{1/2}$  for the same process of the neutral precursor  $p\text{-BrC}_6\text{H}_4\text{N}(\text{CH}_2\text{S})_2\text{Fe}_2\text{CO}_6$  complex; understandably the negative charge of the complex **1** shifted its  $E_{1/2}$  to more cathodic potential relative to its neutral precursor. However, complex **1** shows an onset for HER at  $\sim 350 \text{ mV}$  more positive potential in aqueous medium and exhibits significantly greater HER current at  $-0.5 \text{ V}$  when compared to its precursor complex (Fig. 5C). The greater reactivity for HER of complex **1** result from the fact that its  $\text{Fe}(\text{I})-\text{Fe}(\text{0})$  state is active while for the precursor  $p\text{-BrC}_6\text{H}_4\text{N}(\text{CH}_2\text{S})_2\text{Fe}_2\text{CO}_6$  complex  $\text{Fe}(\text{0})-\text{Fe}(\text{0})$  state is active at these low acid concentrations. At a given potential ( $-0.5 \text{ V vs. NHE}$ ), the HER current is  $10^{3-4}$  times larger for complex **1** relative to its precursor at higher pHs (Fig. S5†). Thus, due to the presence of an anionic  $\text{CN}^-$  ligand, the electron density of the  $\text{Fe}(\text{I})-\text{Fe}(\text{0})$  state of complex **1**, is high enough to allow protonation of the Fe center.



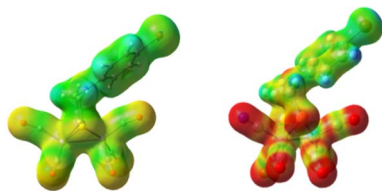


Fig. 12 Electrostatic potential plots of the precursor- $p\text{-BrC}_6\text{H}_4\text{-N}(\text{CH}_2\text{S})_2\text{Fe}_2(\text{CO})_6$  (left) and complex 1 (right).

A pertinent concern of employing a  $\text{CN}^-$  ligand bound to an apparently weak Lewis acid, the reduced  $[\text{Fe}-\text{Fe}]$  cluster, under acidic conditions is the possibility of losing it *via* protonation.<sup>34</sup> Both the XPS and IR data acquired before and after 1 h of electrolysis indicates that the ratio of carbonyl and  $\text{CN}^-$  peaks remain constant *i.e.*,  $\text{CN}^-$  ligands are not preferentially protonated. This is since the electron density of the  $\text{CN}^-$  ligand is strongly delocalized into the cluster due to the presence of the  $\pi$  accepting  $-\text{CO}$  ligands (Fig. 12, right). Similar stabilization of anionic ligand binding to a formally weak Lewis acid centre has been proposed for  $[\text{Fe}-\text{Fe}]$   $\text{H}_2\text{ase}$  and encountered in the mononuclear iron active site in Hmd where the  $-\text{CO}$  and acyl ligands facilitated the delocalization of the electron density of anionic ligands into the active site enhancing their binding affinities.<sup>1,76,104</sup> The synthetic  $[\text{Fe}-\text{Fe}]$  clusters with terminal  $\text{CN}^-$  ligand which were reported to decompose in the presence of acid had at least one of the terminal  $\text{CO}$ 's replaced by weaker  $\pi$  acceptors like phosphine or  $\text{CN}^-$  weakening the charge delocalization.<sup>34</sup> Furthermore, the data obtained from both under aqueous and organic conditions indicate that protonation upon reduction forming the terminal  $\text{Fe}(\text{I})\text{-Fe}(\text{II})\text{-H}$  species with a  $\mu\text{-CO}$  is extremely fast occurring at diffusion controlled rates in aqueous medium. This minimizes the lifetime of  $\text{Fe}(\text{I})\text{-Fe}(\text{0})$  species during catalysis minimizing the possibility of  $\text{CN}^-$  protonolysis during catalysis.

## Conclusions

In summary, a synthetic model of the  $[\text{Fe}-\text{Fe}]$   $\text{H}_2\text{ase}$  bearing ADT and  $\text{CN}^-$  terminal ligands is reported. The presence of  $\text{CN}^-$  raises the  $\text{pK}_\text{a}$  of the cluster allowing HER at mildly acidic pHs at extremely facile diffusion limited rates in aqueous medium. The electron donation from the  $\text{CN}^-$  ligand enables the cluster to catalyze HER from its  $\text{Fe}(\text{I})\text{-Fe}(\text{0})$  state which results in a substantial lowering of overpotential associated with HER catalyzed by similar complexes but without the  $\text{CN}^-$  ligand as these need to be reduced to their  $\text{Fe}(\text{0})\text{-Fe}(\text{0})$  states for them to be able to catalyze HER. *In situ* FTIR-SEC suggest the formation of a terminal hydride species *via* one electron reduction and protonation of the  $\text{Fe}(\text{I})\text{-Fe}(\text{I})$  cluster. Importantly, the  $\text{CN}^-$  ligand is found to remain stable during these experiments.

## Data availability

All data associated with this publication are provided in the ESI.†

## Author contributions

A. N. synthesized the complex and performed characterization of the complex. A. N. and S. D. carried out electrochemical experiments and spectroscopic studies. S. P. and A. N. has performed the IR-SEC experiment. A. R. assisted in DFT-calculations. P. S., S. G. and S. P. recorded the EXAFS data. S. G. D. supervised the work and assisted in the data analysis. A. D. designed the project, assisted in the data analysis wrote the manuscript.

## Conflicts of interest

There are no conflicts to declare.

## Acknowledgements

A. N. thanks IACS for fellowship. S. P. acknowledge CSIR-SRF for fellowship. This work is funded by Department of Science and Technology, India, (DST/TMD/HFC/2K18/90) (A.D.), the US National Institutes of Health grant GM65440 (SPC) and the US DOE OBER (SPC). All X-ray spectroscopy was performed at the Stanford Synchrotron Radiation Light source (SSRL), a national user facility operated by Stanford University on behalf of the DOE OBES. The SSRL Structural Molecular Biology Program is supported by the DOE OBER, and the NIH, National Center for Research Resources, Biomedical Technology Program.

## References

- 1 S. Dey, P. K. Das and A. Dey, *Coord. Chem. Rev.*, 2013, **257**, 42–63.
- 2 R. K. Thauer, A. R. Klein and G. C. Hartmann, *Chem. Rev.*, 1996, **96**, 3031–3042.
- 3 P. M. Vignais and B. Billoud, *Chem. Rev.*, 2007, **107**, 4206–4272.
- 4 J. C. Fontecilla-Camps, A. Volbeda, C. Cavazza and Y. Nicolet, *Chem. Rev.*, 2007, **107**, 4273–4303.
- 5 S. Shima and R. K. Thauer, *Chem. Rec.*, 2007, **7**, 37–46.
- 6 S. Rospert, J. Breitung, K. Ma, B. Schwörer, C. Zirngibl, R. K. Thauer, D. Linder, R. Huber and K. O. Stetter, *Arch. Microbiol.*, 1991, **156**, 49–55.
- 7 M. Y. Darensbourg, E. J. Lyon, X. Zhao and I. P. Georgakaki, *Proc. Natl. Acad. Sci. U. S. A.*, 2003, **100**, 3683–3688.
- 8 M. Frey, *ChemBioChem*, 2002, **3**, 153–160.
- 9 Y. Nicolet, C. Piras, P. Legrand, C. E. Hatchikian and J. C. Fontecilla-Camps, *Structure*, 1999, **7**, 13–23.
- 10 J. W. Peters, W. N. Lanzilotta, B. J. Lemon and L. C. Seefeldt, *Science*, 1998, **282**, 1853–1858.
- 11 Y. Nicolet, A. L. de Lacey, X. Vernède, V. M. Fernandez, E. C. Hatchikian and J. C. Fontecilla-Camps, *J. Am. Chem. Soc.*, 2001, **123**, 1596–1601.
- 12 W. Lubitz, E. Reijerse and M. van Gastel, *Chem. Rev.*, 2007, **107**, 4331–4365.
- 13 C. V. Popescu and E. Münck, *J. Am. Chem. Soc.*, 1999, **121**, 7877–7884.





- 14 A. Adamska, A. Silakov, C. Lambertz, O. Rüdiger, T. Happe, E. Reijerse and W. Lubitz, *Angew Chem. Int. Ed. Engl.*, 2012, **51**, 11458–11462.
- 15 C. Lorent, S. Katz, J. Duan, C. J. Kulka, G. Caserta, C. Teutloff, S. Yadav, U.-P. Apfel, M. Winkler, T. Happe, M. Horch and I. Zebger, *J. Am. Chem. Soc.*, 2020, **142**, 5493–5497.
- 16 M. Haumann and S. T. Stripp, *Acc. Chem. Res.*, 2018, **51**, 1755–1763.
- 17 C. Sommer, A. Adamska-Venkatesh, K. Pawlak, J. A. Birrell, O. Rüdiger, E. J. Reijerse and W. Lubitz, *J. Am. Chem. Soc.*, 2017, **139**, 1440–1443.
- 18 M. W. Ratzloff, J. H. Artz, D. W. Mulder, R. T. Collins, T. E. Furtak and P. W. King, *J. Am. Chem. Soc.*, 2018, **140**, 7623–7628.
- 19 M. L. K. Sanchez, C. Sommer, E. Reijerse, J. A. Birrell, W. Lubitz and R. B. Dyer, *J. Am. Chem. Soc.*, 2019, **141**, 16064–16070.
- 20 J. A. Birrell, V. Pelmeshnikov, N. Mishra, H. Wang, Y. Yoda, K. Tamasaku, T. B. Rauchfuss, S. P. Cramer, W. Lubitz and S. DeBeer, *J. Am. Chem. Soc.*, 2020, **142**, 222–232.
- 21 P. Rodríguez-Maciá, N. Breuer, S. DeBeer and J. A. Birrell, *ACS Catal.*, 2020, **10**, 13084–13095.
- 22 P. Rodríguez-Maciá, K. Pawlak, O. Rüdiger, E. J. Reijerse, W. Lubitz and J. A. Birrell, *J. Am. Chem. Soc.*, 2017, **139**, 15122–15134.
- 23 A. Silakov, B. Wenk, E. Reijerse and W. Lubitz, *Phys. Chem. Chem. Phys.*, 2009, **11**, 6592–6599.
- 24 D. W. Mulder, Y. Guo, M. W. Ratzloff and P. W. King, *J. Am. Chem. Soc.*, 2017, **139**, 83–86.
- 25 E. J. Reijerse, C. C. Pham, V. Pelmeshnikov, R. Gilbert-Wilson, A. Adamska-Venkatesh, J. F. Siebel, L. B. Gee, Y. Yoda, K. Tamasaku, W. Lubitz, T. B. Rauchfuss and S. P. Cramer, *J. Am. Chem. Soc.*, 2017, **139**, 4306–4309.
- 26 V. Pelmeshnikov, J. A. Birrell, C. C. Pham, N. Mishra, H. Wang, C. Sommer, E. Reijerse, C. P. Richers, K. Tamasaku, Y. Yoda, T. B. Rauchfuss, W. Lubitz and S. P. Cramer, *J. Am. Chem. Soc.*, 2017, **139**, 16894–16902.
- 27 M. Winkler, M. Senger, J. Duan, J. Esselborn, F. Wittkamp, E. Hofmann, U.-P. Apfel, S. T. Stripp and T. Happe, *Nat. Commun.*, 2017, **8**, 16115.
- 28 C.-H. Hsieh, Ö. F. Erdem, S. D. Harman, M. L. Singleton, E. Reijerse, W. Lubitz, C. V. Popescu, J. H. Reibenspies, S. M. Brothers, M. B. Hall and M. Y. Darensbourg, *J. Am. Chem. Soc.*, 2012, **134**, 13089–13102.
- 29 M. T. Olsen, M. Bruschi, L. De Gioia, T. B. Rauchfuss and S. R. Wilson, *J. Am. Chem. Soc.*, 2008, **130**, 12021–12030.
- 30 A. K. Justice, M. J. Nilges, T. B. Rauchfuss, S. R. Wilson, L. De Gioia and G. Zampella, *J. Am. Chem. Soc.*, 2008, **130**, 5293–5301.
- 31 A. T. Fiedler and T. C. Brunold, *Inorg. Chem.*, 2005, **44**, 9322–9334.
- 32 S. Amanullah, P. Saha, A. Nayek, M. E. Ahmed and A. Dey, *Chem. Soc. Rev.*, 2021, **50**, 3755–3823.
- 33 V. Artero, G. Berggren, M. Atta, G. Caserta, S. Roy, L. Pecqueur and M. Fontecave, *Acc. Chem. Res.*, 2015, **48**, 2380–2387.
- 34 F. Gloaguen, J. D. Lawrence and T. B. Rauchfuss, *J. Am. Chem. Soc.*, 2001, **123**, 9476–9477.
- 35 J. T. Kleinhaus, F. Wittkamp, S. Yadav, D. Siegmund and U.-P. Apfel, *Chem. Soc. Rev.*, 2021, **50**, 1668–1784.
- 36 T. B. Rauchfuss, *Acc. Chem. Res.*, 2015, **48**, 2107–2116.
- 37 C. Tard and C. J. Pickett, *Chem. Rev.*, 2009, **109**, 2245–2274.
- 38 T. Liu and M. Y. Darensbourg, *J. Am. Chem. Soc.*, 2007, **129**, 7008–7009.
- 39 J. M. Camara and T. B. Rauchfuss, *Nat. Chem.*, 2012, **4**, 26–30.
- 40 F. Gloaguen and T. B. Rauchfuss, *Chem. Soc. Rev.*, 2009, **38**, 100–108.
- 41 A. Nayek, M. E. Ahmed, S. Samanta, S. Dinda, S. Patra, S. G. Dey and A. Dey, *J. Am. Chem. Soc.*, 2022, **144**, 8402–8429.
- 42 M. Razavet, S. J. Borg, S. J. George, S. P. Best, S. A. Fairhurst and C. J. Pickett, *Chem. Commun.*, 2002, 700–701.
- 43 M. E. Carroll, B. E. Barton, T. B. Rauchfuss and P. J. Carroll, *J. Am. Chem. Soc.*, 2012, **134**, 18843–18852.
- 44 A. Silakov, J. L. Shaw, E. J. Reijerse and W. Lubitz, *J. Am. Chem. Soc.*, 2010, **132**, 17578–17587.
- 45 O. F. Erdem, L. Schwartz, M. Stein, A. Silakov, S. Kaur-Ghumaan, P. Huang, S. Ott, E. J. Reijerse and W. Lubitz, *Angew Chem. Int. Ed. Engl.*, 2011, **50**, 1439–1443.
- 46 H. J. Redman, P. Huang, M. Haumann, M. H. Cheah and G. Berggren, *Dalton Trans.*, 2022, **51**, 4634–4643.
- 47 Ö. F. Erdem, M. Stein, S. Kaur-Ghumaan, E. J. Reijerse, S. Ott and W. Lubitz, *Chem.–A Euro. J.*, 2013, **19**, 14566–14572.
- 48 A. Silakov, M. T. Olsen, S. Sproules, E. J. Reijerse, T. B. Rauchfuss and W. Lubitz, *Inorg. Chem.*, 2012, **51**, 8617–8628.
- 49 A. Le Cloirec, S. P. Best, S. Borg, S. C. Davies, D. J. Evans, D. L. Hughes and C. J. Pickett, *Chem. Commun.*, 1999, **1**, 2285–2286.
- 50 E. J. Lyon, I. P. Georgakaki, J. H. Reibenspies and M. Y. Darensbourg, *Angew. Chem., Int. Ed.*, 1999, **38**, 3178–3180.
- 51 F. Gloaguen, J. D. Lawrence, M. Schmidt, S. R. Wilson and T. B. Rauchfuss, *J. Am. Chem. Soc.*, 2001, **123**, 12518–12527.
- 52 C. Esmieu and G. Berggren, *Dalton Trans.*, 2016, **45**, 19242–19248.
- 53 J. D. Lawrence, H. Li, T. B. Rauchfuss, M. Bénard and M.-M. Rohmer, *Angew. Chem., Int. Ed.*, 2001, **40**, 1768–1771.
- 54 B. C. Manor, M. R. Ringenberg and T. B. Rauchfuss, *Inorg. Chem.*, 2014, **53**, 7241–7247.
- 55 G. Berggren, A. Adamska, C. Lambertz, T. R. Simmons, J. Esselborn, M. Atta, S. Gambarelli, J.-M. Mouesca, E. Reijerse, W. Lubitz, T. Happe, V. Artero and M. Fontecave, *Nature*, 2013, **499**, 66–69.
- 56 J. Esselborn, C. Lambertz, A. Adamska-Venkatesh, T. Simmons, G. Berggren, J. Noth, J. Siebel, A. Hemschemeier, V. Artero, E. Reijerse, M. Fontecave, W. Lubitz and T. Happe, *Nat. Chem. Biol.*, 2013, **9**, 607–609.
- 57 R. Gilbert-Wilson, J. F. Siebel, A. Adamska-Venkatesh, C. C. Pham, E. Reijerse, H. Wang, S. P. Cramer, W. Lubitz



- and T. B. Rauchfuss, *J. Am. Chem. Soc.*, 2015, **137**, 8998–9005.
- 58 J. F. Siebel, A. Adamska-Venkatesh, K. Weber, S. Rumpel, E. Reijerse and W. Lubitz, *Biochemistry*, 2015, **54**, 1474–1483.
- 59 J. Esselborn, N. Muraki, K. Klein, V. Engelbrecht, N. Metzler-Nolte, U.-P. Apfel, E. Hofmann, G. Kurisu and T. Happe, *Chem. Sci.*, 2016, **7**, 959–968.
- 60 A. Adamska-Venkatesh, S. Roy, J. F. Siebel, T. R. Simmons, M. Fontecave, V. Artero, E. Reijerse and W. Lubitz, *J. Am. Chem. Soc.*, 2015, **137**, 12744–12747.
- 61 C. Esmieu, M. Guo, H. J. Redman, M. Lundberg and G. Berggren, *Dalton Trans.*, 2019, **48**, 2280–2284.
- 62 A. S. Pandey, T. V. Harris, L. J. Giles, J. W. Peters and R. K. Szilagyi, *J. Am. Chem. Soc.*, 2008, **130**, 4533–4540.
- 63 J. C. Lansing, J. M. Camara, D. E. Gray and T. B. Rauchfuss, *Organometallics*, 2014, **33**, 5897–5906.
- 64 D. J. Crouthers, J. A. Denny, R. D. Bethel, D. G. Munoz and M. Y. Darensbourg, *Organometallics*, 2014, **33**, 4747–4755.
- 65 M. Wang, L. Chen and L. Sun, *Energy Environ. Sci.*, 2012, **5**, 6763–6778.
- 66 B. Kumar, M. Beyler, C. P. Kubiak and S. Ott, *Chem.–A Euro. J.*, 2012, **18**, 1295–1298.
- 67 R. Mejia-Rodriguez, D. Chong, J. H. Reibenspies, M. P. Soriaga and M. Y. Darensbourg, *J. Am. Chem. Soc.*, 2004, **126**, 12004–12014.
- 68 G. Si, W.-G. Wang, H.-Y. Wang, C.-H. Tung and L.-Z. Wu, *Inorg. Chem.*, 2008, **47**, 8101–8111.
- 69 C. Esmieu and G. Berggren, *Dalton Trans.*, 2016, **45**, 19242–19248.
- 70 S. Dey, A. Rana, S. G. Dey and A. Dey, *ACS Catal.*, 2013, **3**, 429–436.
- 71 F. Quentel, G. Passard and F. Gloaguen, *Energy Environ. Sci.*, 2012, **5**, 7757–7761.
- 72 C. Di Giovanni, W. A. Wang, S. Nowak, J. M. Grenèche, H. Lecoq, L. Mouton, M. Giraud and C. Tard, *ACS Catal.*, 2014, **4**, 681–687.
- 73 S. Ott, M. Kritikos, B. Åkermærk, L. Sun and R. Lomoth, *Angew. Chem., Int. Ed.*, 2004, **43**, 1006–1009.
- 74 S. Dey, A. Rana, D. Crouthers, B. Mondal, P. K. Das, M. Y. Darensbourg and A. Dey, *J. Am. Chem. Soc.*, 2014, **136**, 8847–8850.
- 75 M. E. Ahmed, S. Dey, M. Y. Darensbourg and A. Dey, *J. Am. Chem. Soc.*, 2018, **140**, 12457–12468.
- 76 H. J. Redman, P. Huang, M. Haumann, M. H. Cheah and G. Berggren, *Dalton Trans.*, 2022, **51**, 4634–4643.
- 77 J. T. Kleinhaus, F. Wittkamp, S. Yadav, D. Siegmund and U.-P. Apfel, *Chem. Soc. Rev.*, 2021, **50**, 1668–1784.
- 78 T. B. Rauchfuss, *Acc. Chem. Res.*, 2015, **48**, 2107–2116.
- 79 C. A. Boyke, J. I. van der Vlugt, T. B. Rauchfuss, S. R. Wilson, G. Zampella and L. De Gioia, *J. Am. Chem. Soc.*, 2005, **127**, 11010–11018.
- 80 F. Gloaguen, J. D. Lawrence and T. B. Rauchfuss, *J. Am. Chem. Soc.*, 2001, **123**, 9476–9477.
- 81 A. Le Cloirec, S. C. Davies, D. J. Evans, D. L. Hughes, C. J. Pickett, S. P. Best and S. Borg, *Chem. Commun.*, 1999, 2285–2286.
- 82 F. Gloaguen, J. D. Lawrence, M. Schmidt, S. R. Wilson and T. B. Rauchfuss, *J. Am. Chem. Soc.*, 2001, **123**, 12518–12527.
- 83 L. C. Song, Z. Y. Yang, H. Z. Bian and Q. M. Hu, *Organometallics*, 2004, **23**, 3082–3084.
- 84 A. D. Becke, *Phys. Rev. A*, 1988, **38**, 3098–3100.
- 85 A. D. Becke, *J. Chem. Phys.*, 1993, **98**, 5648–5652.
- 86 J. P. Perdew, *Phys. Rev. B*, 1986, **33**, 8822–8824.
- 87 A. Adamska-Venkatesh, D. Krawietz, J. Siebel, K. Weber, T. Happe, E. Reijerse and W. Lubitz, *J. Am. Chem. Soc.*, 2014, **136**, 11339–11346.
- 88 S. J. Borg, J. W. Tye, M. B. Hall and S. P. Best, *Inorg. Chem.*, 2007, **46**, 384–394.
- 89 B. Sieklucka, R. Dziembaj and S. Witkowski, *Inorg. Chim. Acta*, 1991, **187**, 5–8.
- 90 B. Mondal, K. Sengupta, A. Rana, A. Mahammed, M. Botoshansky, S. Ghosh Dey, Z. Gross and A. Dey, *Inorg. Chem.*, 2013, **52**, 3381–3387.
- 91 A. Le Goff, V. Artero, B. Jousset, P. D. Tran, N. Guillet, R. Métayé, A. Fihri, S. Palacin and M. Fontecave, *Science*, 2009, **326**, 1384–1387.
- 92 A. Lasia, *Int. J. Hydrogen Energy*, 2019, **44**, 19484–19518.
- 93 T. Shinagawa, A. T. Garcia-Esparza and K. Takanabe, *Sci. Rep.*, 2015, **5**, 1–21.
- 94 J. O. Bockris and E. C. Potter, *J. Electrochem. Soc.*, 1952, **99**, 169.
- 95 M. K. Harb, U.-P. Apfel, J. Kübel, H. Görls, G. A. N. Felton, T. Sakamoto, D. H. Evans, R. S. Glass, D. L. Lichtenberger, M. El-khateeb and W. Weigand, *Organometallics*, 2009, **28**(23), 6666–6675.
- 96 V. Fourmond, P.-A. Jacques, M. Fontecave and V. Artero, *Inorg. Chem.*, 2010, **49**, 10338–10347.
- 97 A. Aster, S. Wang, M. Mirmohades, C. Esmieu, G. Berggren, L. Hammarström and R. Lomoth, *Chem. Sci.*, 2019, **10**, 5582–5588.
- 98 J. A. Wright, L. Webster, A. Jablonskytė, P. M. Woi, S. K. Ibrahim and C. J. Pickett, *Faraday Discuss.*, 2011, **148**, 359–371.
- 99 M. E. Ahmed, A. Nayek, A. Križan, N. Coutard, A. Morozan, S. Ghosh Dey, R. Lomoth, L. Hammarström, V. Artero and A. Dey, *J. Am. Chem. Soc.*, 2022, **144**, 3614–3625.
- 100 J. A. Birrell, V. Pelmeshnikov, N. Mishra, H. Wang, Y. Yoda, K. Tamasaku, T. B. Rauchfuss, S. P. Cramer, W. Lubitz and S. DeBeer, *J. Am. Chem. Soc.*, 2020, **142**, 222–232.
- 101 J. Rosenthal and D. G. Nocera, *Acc. Chem. Res.*, 2007, **40**, 543–553.
- 102 D. R. Weinberg, C. J. Gagliardi, J. F. Hull, C. F. Murphy, C. A. Kent, B. C. Westlake, A. Paul, D. H. Ess, D. G. McCafferty and T. J. Meyer, *Chem. Rev.*, 2012, **112**, 4016–4093.
- 103 B. E. Conway and B. V. Tilak, *Electrochim. Acta*, 2002, **47**, 3571–3594.
- 104 A. Dey, *J. Am. Chem. Soc.*, 2010, **132**, 13892–13901.

